PHYSICAL REVIEW A VOLUME 36, NUMBER 5 SEPTEMBER 1, 1987

Three-dimensional nonlinear analysis of free-electron-laser amplifiers with planar wigglers

H. P. Freund
Science Applications International Corporation, McLean, Virginia 22102

H. Bluem
Department of Electrical Engineering, University of Maryland, College Park, Maryland 20742

C. L. Chang
Science Applications International Corporation, McLean, Virginia 22102

(Received 23 March 1987)

The nonlinear evolution of the free-electron-laser (FEL) amplifier is investigated numerically for a configuration consisting of a planar wiggler with parabolically tapered pole pieces. A set of coupled nonlinear differential equations is derived in three dimensions which governs the self-consistent evolution of the TE and TM modes in a loss-free rectangular waveguide as well as the trajectories of an ensemble of electrons. The initial conditions are chosen to model the injection of a cylindrically symmetric electron beam into the wiggler by means of a region with an adiabatically tapered wiggler amplitude, and the effect of an initial beam momentum spread is included in the formulation. Both self-field and space-charge effects have been neglected, and the analysis is valid for the high-gain Compton regime. In addition, the phase stability of the FEL amplifier against fluctuations in the beam voltage, the enhancement of the efficiency by means of a tapered wiggler amplitude, and harmonic generation are also studied. Numerical simulations are conducted to model a 35-GHz amplifier with an electron beam energy of 3.5 MeV, and good agreement is found between the simulation and an experiment conducted by Orzechowski and co-workers. Significantly, the results indicate that a tapered wiggler configuration is somewhat less sensitive to the beam thermal spread than a uniform wiggler system.

I. INTRODUCTION

The free-electron laser (FEL) and the ubitron[1] have been successfully demonstrated as radiation sources over a broad frequency range from the microwave[1-13] through the optical[14-21] spectra. The distinction between the ubitron and the FEL is not well defined in the literature; however, we find it convenient to differentiate between the FEL and the ubitron primarily on the basis of the electron-beam energy. As such, we refer to those devices as ubitrons when the beam energy is below 500 keV. Although this definition is somewhat arbitrary, operation at these energies generally involves frequencies close to the waveguide cutoff of the device, and the ubitron may be thought of as a weakly relativistic FEL operated as a microwave tube. In either case, however, the physical-interaction mechanism is the same, and relies on a periodically rippled magnetic field (referred to as the wiggler field) to induce an oscillatory motion in the electron beam. The interaction between the transverse component of the oscillatory motion and the radiation field results in an axial bunching of the electron beam which is the source of the instability. This axial-bunching mechanism can be thought of as the result of the ponderomotive potential formed by the beating of the wiggler and radiation fields. The precise form for the wiggler field can take a variety of configurations, and ubitrons and FEL's have been constructed using both helically[2-8,10-12,14,15] and linearly[1,9,13,16-21] polarized wiggler fields. In addition, a wiggler configuration has been proposed which makes use of a rotating quadrupole design.[22]

The motivation for the present work is to develop a nonlinear theory and simulation code for a ubitron or FEL amplifier based upon a linearly polarized wiggler field. The advantage of a planar wiggler design over that of a helical configuration is ease of construction and modification. Linearly polarized wigglers are readily constructed from permanent magnet arrays which can be easily adjusted to a tapered wiggler configuration. In this paper we derive a fully three-dimensional nonlinear analysis of the FEL and the ubitron for the planar wiggler configuration. The analysis follows that described previously for a helical wiggler configuration,[23-27] and involves the derivation of a set of coupled nonlinear differential equations which self-consistently describe the evolution of both an ensemble of electrons and the electromagnetic fields in a rectangular waveguide. Space-charge fields are neglected in the analysis; therefore, the treatment is applicable to the high-gain Compton (or strong-pump) regime. The nonlinear current which mediates the interaction is computed from the microscopic behavior of the electrons by means of an average of the electron phases relative to the ponderomotive wave formed by the beating of the wiggler and radiation fields. The detailed wiggler

model we employ includes the effect of parabolically tapered pole pieces in order to provide for electron focusing in the plane of the bulk wiggler motion. Further, the injection of the electron beam into the wiggler field is modeled by allowing the wiggler amplitude to increase adiabatically from zero to a constant level. The procedure used also permits the inclusion of an arbitrary taper of the wiggler amplitude for the purpose of the enhancement of the interaction efficiency. The overlap between the electron beam and the transverse mode structure of the TE and TM modes is included in a self-consistent manner, so that no arbitrary "filling factor" need be included in the analysis. Since the problem of interest is that of a FEL or ubitron amplifier, only single-frequency propagation is considered. This permits an average over a wave period to be performed which eliminates the fast-time-scale phenomena from the formulation, and results in a great increase in computational efficiency over a full-scale particle-in-cell simulation.

In organization of this paper is as follows. The general equations are derived in Sec. II. The numerical solution to the dynamical equations is given in Sec. IV, in which a particular example is treated in depth which corresponds to a recent experiment by Orzechowski and co-workers.[13] Three distinct waveguide modes are found to grow in simulation, and we consider each of these modes in detail including the bandwidths and relative growth rates and saturation efficiencies. Also considered are the effects of (1) variations in the length of the entry region on the saturation efficiency, (2) an initial momentum spread in the electron beam (i.e., prior to the injection into the wiggler), (3) the scaling of the efficiency with beam current, and (4) the enhancement of the interaction efficiency through a linearly tapered wiggler amplitude. These issues are treated in an abstract manner in Sec. III because the analysis does not correspond to all aspects of the experimental configuration. However, a comparison between the simulation and the experiment is made in Sec. IV in which we give a summary and discussion.

II. GENERAL FORMULATION

The configuration we consider is that of a relativistic electron beam propagating through a loss-free rectangular waveguide in the presence of a linearly polarized wiggler magnetic field. The wiggler-field model that we employ is that encountered when the individual magnets in the wiggler have parabolically tapered pole faces, which provides for electron-beam focusing in the plane of the principal wiggler motion. This technique was first employed experimentally by Phillips.[1] A detailed analysis of the magnetic field produced by a wiggler with parabolically tapered pole pieces was undertaken by Scharlemann,[28] who showed that the wiggler field is of the form

$$\mathbf{B}_w(\mathbf{x})=B_w\left\{\cos(k_w z)\left[\sinh\left[\frac{k_w x}{\sqrt{2}}\right]\sinh\left[\frac{k_w y}{\sqrt{2}}\right]\hat{\mathbf{e}}_x+\cosh\left[\frac{k_w x}{\sqrt{2}}\right]\cosh\left[\frac{k_w y}{\sqrt{2}}\right]\hat{\mathbf{e}}_y\right]-\sqrt{2}\cosh\left[\frac{k_w x}{\sqrt{2}}\right]\sinh\left[\frac{k_w y}{\sqrt{2}}\right]\sin(k_w z)\hat{\mathbf{e}}_z\right\}, \tag{1}$$

where B_w denotes the wiggler amplitude, and $k_w(\equiv 2\pi/\lambda_w)$ is the wiggler wave number. We model the injection of the electron beam into the wiggler by allowing the wiggler amplitude to increase adiabatically from zero to a constant level over N_w wiggler periods. In addition, since we intend to study efficiency enhancement by means of a tapered wiggler, the wiggler amplitude will be tapered starting at some point z_0 downstream from the entry region in a linear fashion. To this end, we choose

$$B_w(z)=\begin{cases}B_w\sin^2(k_w z/4N_w), & 0\le z\le N_w\lambda_w\\ B_w, & N_w\lambda_w<z\le z_0\\ B_w[1+\epsilon_w k_w(z-z_0)], & z>z_0\end{cases} \tag{2}$$

where

$$\epsilon_w\equiv\frac{1}{k_w}\frac{d}{dz}\ln B_w \tag{3}$$

describes the slope of the taper. Since the fringing fields associated with the tapered wiggler amplitude are neglected, this representation is strictly valid only if the slope of the taper is small. Within the entry region this implies that N_w must be large, while for $z>z_0$ we must require that $|\epsilon_w|\ll 1$.

The boundary conditions at the waveguide wall may be satisfied by expanding the vector potential in terms of the orthogonal basis functions of the vacuum waveguide. Thus, we write the vector potential of the radiation in the form

$$\delta\mathbf{A}(\mathbf{x},t)=\sum_{l,n=0}^{\infty}{}'\,\delta A_{ln}(z)\mathbf{e}_{ln}^{(1)}(x,y)\cos\alpha \tag{4}$$

for the TE modes, and

$$\delta\mathbf{A}(\mathbf{x},t)=\sum_{l,n=1}^{\infty}\delta A_{ln}(z)\left[\mathbf{e}_{ln}^{(2)}(x,y)\cos\alpha+\frac{k_{ln}}{k}\sin\left[\frac{l\pi X}{a}\right]\times\sin\left[\frac{n\pi Y}{b}\right]\sin\alpha\hat{\mathbf{e}}_z\right] \tag{5}$$

for the TM modes, where for frequency ω and wave number $k(z)$,

$$\alpha\equiv\int_0^z dz'k(z')-\omega t\ . \tag{6}$$

In addition, $\sum'$ indicates that l and n are not both zero, and

$$\mathbf{e}_{\ln}^{(1)}(x,y)\equiv\frac{n\pi}{k_{\ln}b}\cos\left[\frac{l\pi X}{a}\right]\sin\left[\frac{n\pi Y}{b}\right]\hat{\mathbf{e}}_x - \frac{l\pi}{k_{\ln}a}\sin\left[\frac{l\pi X}{a}\right]\cos\left[\frac{n\pi Y}{b}\right]\hat{\mathbf{e}}_y , \tag{7}$$

$$\mathbf{e}_{\ln}^{(2)}(x,y)\equiv\frac{l\pi}{k_{\ln}a}\cos\left[\frac{l\pi X}{a}\right]\sin\left[\frac{n\pi Y}{b}\right]\hat{\mathbf{e}}_x + \frac{n\pi}{k_{\ln}b}\sin\left[\frac{l\pi X}{a}\right]\cos\left[\frac{n\pi Y}{b}\right]\hat{\mathbf{e}}_y \tag{8}$$

are the polarization vectors. In this representation the waveguide is assumed to be centered at the origin and bounded by $-a/2\le x\le a/2$ and $-b/2\le y\le b/2$. As a consequence, $X\equiv x+a/2$, $Y\equiv y+b/2$, and

$$k_{\ln}\equiv\pi\left[\frac{l^2}{a^2}+\frac{n^2}{b^2}\right]^{1/2} \tag{9}$$

denotes the cutoff wave vector. It is implicitly assumed that both $\delta A_{\ln}(z)$ and $k(z)$ vary slowly over a wave period.

The microscopic source current can be written as the following sum over individual particle trajectories:

$$\delta\mathbf{J}(\mathbf{x},t)=-e\sum_{i=1}^{N_T}\mathbf{v}_i(z;\mathbf{p}_{i0},x_{i0},y_{i0},t_{i0})\times\delta[\mathbf{x}_\perp-\mathbf{x}_{\perp i}(z;\mathbf{p}_{i0},x_{i0},y_{i0},t_{i0})]\times\frac{\delta[t-\tau_i(z;\mathbf{p}_{i0},x_{i0},y_{i0},t_{i0})]}{|v_{zi}(z;\mathbf{p}_{i0},x_{i0},y_{i0},t_{i0})|} , \tag{10}$$

where L is the length of the interaction region, N_T is the total number of electrons, n_b is the average electron density, $\mathbf{v}_i(z;\mathbf{p}_{i0},x_{i0},y_{i0},t_{i0})$ is the velocity of the ith electron at position z which entered the interaction region (i.e., crossed the $z=0$ plane) at time t_{i0} and transverse position (x_{i0},y_{i0}) with momentum $\mathbf{p}_{i0}$, and

$$\tau_i(z;\mathbf{p}_{i0},x_{i0},y_{i0},t_{i0})\equiv t_{i0}+\int_0^z\frac{dz'}{v_{zi}(z';\mathbf{p}_{i0},x_{i0},y_{i0},t_{i0})} . \tag{11}$$

This discrete sum over particles can be replaced by an integration over the initial conditions, and we write

$$\delta\mathbf{J}(\mathbf{x},t)=-en_b\int d\mathbf{p}_0 v_{z0}F_0(\mathbf{p})\int\int_{A_g}dx_0dy_0\sigma_\perp(x_0,y_0)\int_{-T/2}^{T/2}dt_0\sigma_\parallel(t_0)\mathbf{v}(z;\mathbf{p}_0,x_0,y_0,t_0)\times\delta[\mathbf{x}_\perp-\mathbf{x}_\perp(z;\mathbf{p}_0,x_0,y_0,t_0)]\frac{\delta[t-\tau(z;\mathbf{p}_0,x_0,y_0,t_0)]}{|v_z(z;\mathbf{p}_0,x_0,y_0,t_0)|} , \tag{12}$$

where v_{z0} is the initial axial velocity, $A_g\equiv ab$ is the area of the waveguide, $T\equiv L/\langle v_{z0}\rangle$, and $\sigma_\perp(x_0,y_0)$, $\sigma_\parallel(t_0)$, and F_0 $(\mathbf{p}_0)$ describe the distributions of the initial conditions subject to the normalizations (A_b is the cross sectional area of the beam)

$$\int\int_{A_g}dx_0dy_0\sigma_\perp(x_0,y_0)=A_b , \tag{13}$$

$$\int_{-T/2}^{T/2}dt_0\sigma_\parallel(t_0)=T , \tag{14}$$

and

$$\int d\mathbf{p}_0F_0(\mathbf{p}_0)=1 . \tag{15}$$

Substitution of the microscopic fields and the source current into Maxwell's equations yields the equations which govern the evolution of the radiation amplitude and wave number. The procedure is formally identical to that described previously for the helical wiggler, cylindrical waveguide configuration,[23] and involves a modal orthogonalization in the transverse coordinates. In addition, a quasistatic assumption is made in the sense that particles which enter the interaction region at times t_0 separated by integral multiples of a wave period are assumed to execute identical trajectories. As a result, $\mathbf{v}(z;\mathbf{p}_0,x_0,y_0,t_0+2\pi N/\omega)=\mathbf{v}(z;\mathbf{p}_0,x_0,y_0,t_0)$ for the integer N, and a time average over a wave period can be performed which permits consideration of a single "beamlet" that includes electrons which enter the interaction region within one ponderomotive (or wave) period.[29] This greatly improves the computational efficiency. It should be remarked that the ponderomotive phase of each particle is followed self-consistently in the analysis, so that while the beamlet is initially distributed over one ponderomotive wave, the final state may describe an electron distribution which has become trapped within several ponderomotive buckets. In view of this, the equations which govern the evolution of the $\mathrm{TE}_{\ln}$ mode are

$$\frac{d^2}{dz^2}\delta a_{\ln}+\left[\frac{\omega^2}{c^2}-k^2-k_{\ln}^2\right]\delta a_{\ln}=8\frac{\omega_b^2}{c^2}F_{\ln}\left\langle\frac{\cos\alpha}{|v_z|}\mathbf{e}_{\ln}^{(1)}\cdot\mathbf{v}\right\rangle , \tag{16}$$

and

$$2k^{1/2}\frac{d}{dz}(k^{1/2}\delta a_{\ln})=-8\frac{\omega_b^2}{c^2}F_{\ln}\left\langle\frac{\sin\alpha}{|v_z|}\mathbf{e}_{\ln}^{(1)}\cdot\mathbf{v}\right\rangle , \tag{17}$$

where $\delta a_{\ln}\equiv e\delta A_{\ln}/mc^2$, $\omega_b^2\equiv 4\pi e^2n_b/m$, $\mathbf{v}$ is the instantaneous velocity, and $F_{\ln}\equiv\frac{1}{2}$ when either $l=0$ or $n=0$ and unity otherwise. For the $\mathrm{TM}_{\ln}$ mode we obtain a similar result,

$$\frac{d^2}{dz^2}\delta a_{ln}+\left[1+\frac{k_{ln}^2}{k^2}\right]\left[\frac{\omega^2}{c^2}-k^2-k_{ln}^2\right]\delta a_{ln}=8\frac{\omega_b^2}{c^2}\left\langle\frac{\cos\alpha}{|v_z|}\mathbf{e}_{ln}^{(2)}\cdot\mathbf{v}+\frac{v_z}{|v_z|}\frac{k_{ln}}{k}\sin\left[\frac{l\pi X}{a}\right]\sin\left[\frac{n\pi Y}{b}\right]\sin\alpha\right\rangle , \tag{18}$$

and

$$2\left[k+\frac{k_{ln}^2}{k}\right]^{1/2}\frac{d}{dz}\left[\left[k+\frac{k_{ln}^2}{k}\right]^{1/2}\delta a_{ln}\right]=-8\frac{\omega_b^2}{c^2}\left\langle\frac{\sin\alpha}{|v_z|}\mathbf{e}_{ln}^{(2)}\cdot\mathbf{v}-\frac{v_z}{|v_z|}\frac{k_{ln}}{k}\sin\left[\frac{l\pi X}{a}\right]\sin\left[\frac{n\pi Y}{b}\right]\cos\alpha\right\rangle . \tag{19}$$

Observe that there is no nontrivial TM mode solution when either $l=0$ or $n=0$.

The averaging operator $\langle(\cdots)\rangle$ is defined over the initial conditions of the beam (note that the instantaneous positions and momenta of the electrons are implicit functions of the initial conditions) and includes the effect of an *initial* momentum spread by means of the distribution function

$$F_0(\mathbf{p}_0)=A\exp[-(p_{z0}-p_0)^2/\Delta p_z^2]\delta(p_0^2-p_{\perp 0}^2-p_{z0}^2)H(p_{z0}) , \tag{20}$$

where p_0 and Δp_z describe the initial bulk momentum and momentum spread of the beam, $H(x)$ is the Heaviside function, and the normalization constant is

$$A\equiv\left[\pi\int_0^{p_0}dp_{z0}\exp[-(p_{z0}-p_0)^2/\Delta p_z^2]\right]^{-1} . \tag{21}$$

Observe that the distribution is *monoenergetic,* but contains a pitch angle spread which describes an *axial energy spread* (as well as a transverse energy spread) given approximately by

$$\frac{\Delta\gamma_z}{\gamma_0}\simeq 1-\left[1+2(\gamma_0^2-1)\frac{\Delta p_z}{p_0}\right]^{-1/2} , \tag{22}$$

where $\gamma_0\equiv(1+p_0^2/m^2c^2)^{1/2}$. There is no fundamental difficulty in the inclusion of an overall energy spread in the analysis; however, the additional degree of freedom requires an increased number of particles in the simulation. The δ function allows us to perform one of the momentum-space integrals analytically, and to write the averaging operator in the form

$$\langle(\cdots)\rangle\equiv\frac{A}{2\pi ab}\int_0^{2\pi}d\phi_0\int_0^{p_0}dp_{z0}\beta_{z0}\exp[-(p_{z0}-p_0)^2/\Delta p_z^2]\int_{-\pi}^{\pi}d\psi_0\sigma_{\parallel}(\psi_0)\int_{-a/2}^{a/2}dx_0\int_{-b/2}^{b/2}dy_0\sigma_{\perp}(x_0,y_0)(\cdots) , \tag{23}$$

where $\psi_0(\equiv-\omega t_0)$ is the initial ponderomotive phase, $\phi_0\equiv\tan^{-1}(p_{y0}/p_{x0})$, and $\beta_{z0}\equiv v_{z0}/c$. It is important to recognize that this average includes the effect of the overlap between the electron beam and the transverse mode structure of the radiation field in a self-consistent way.

The phase variation of each mode can be analyzed by the addition of an equation to integrate the relative phase

$$\Phi(z)\equiv\int_0^z dz'[k(z')-k_0] , \tag{24}$$

where $k_0\equiv(\omega^2/c^2-k_{ln}^2)^{1/2}$ is the wave number of the vacuum guide. Since the departure of $k(z)$ from the vacuum wave number describes the effect of the wave-particle interaction, $\Phi(z)$ represents a measure of the dielectric effect of the FEL interaction. Thus, we integrate the additional equation

$$\frac{d}{dz}\Phi=k-k_0 , \tag{25}$$

for both the TE and TM modes.

In order to complete the formulation, the electron-orbit equations must also be specified. Since we describe an amplifier model, we choose to integrate in z and write the Lorentz force equations in the form

$$v_z\frac{d}{dz}\mathbf{p}=-e\delta\mathbf{E}_{ln}-\frac{e}{c}\mathbf{v}\times(\mathbf{B}_w+\delta\mathbf{B}_{ln}) , \tag{26}$$

where $\mathbf{B}_w$ is given by Eqs. (1) and (2) and the radiation fields are given by the vector potentials

$$\delta\mathbf{E}_{ln}=-\frac{1}{c}\frac{\partial}{\partial t}\delta\mathbf{A}_{ln},\quad \delta\mathbf{B}_{ln}=\nabla\times\delta\mathbf{A}_{ln} . \tag{27}$$

Finally, the electron coordinates obey the equations

$$v_z\frac{d}{dz}x=v_x , \tag{28}$$

$$v_z\frac{d}{dz}y=v_y , \tag{29}$$

and

$$\frac{d}{dz}\psi=k+k_w-\frac{\omega}{v_z} \tag{30}$$

describes the evolution of ponderomotive phase

$$\psi=\psi_0+\int_0^z dz'\left[k+k_w-\frac{\omega}{v_z}\right] . \tag{31}$$

III. NUMERICAL ANALYSIS

The set of coupled differential equations described in Sec. II is solved for an amplifier configuration in which a single mode of frequency ω is injected into the system at

$z=0$. The dynamical equations [Eqs. (16)–(19) and (25)] for the fields can be reduced to a set of four first-order ordinary differential equations for δa_{ln}, $\Gamma_{ln}[\equiv k_w^{-1} d(\ln \delta a_{ln})/dz]$, k, and the relative phase Φ. Hence, the numerical resolution of the problem consists in the simultaneous solution of $6N_T+4$ first-order ordinary differential equations, where N_T is the number of electrons. The algorithm we employ is the fourth-order Runge-Kutta-Gill technique. While this technique is somewhat less stable than the fourth-order Adams-Moulton predictor-corrector scheme, it has the advantage of being less memory intensive. Indeed, the requirements placed on the available size of computer memories represents a critical practical limitation when momentum spread is included. The averages in Eqs. (16)–(19) are performed by means of an Nth-order Gaussian quadrature technique in each of the variables $(x_0, y_0, \psi_0, p_{z0}, \phi_0)$.

The initial conditions on the radiation field are chosen such that $\Gamma_{ln}(z=0)=0$, $k(z=0)=k_0$, and $\Phi(z=0)=0$ for an arbitrary initial power level. Observe that the time-averaged Poynting flux P_{ln} for the waveguide modes is related to the field amplitude by the relation

$$P_{ln}=\frac{m^2c^4}{32e^2}\frac{ab}{\pi F_{ln}}\omega k \delta a_{ln}^2 \tag{32}$$

for the TE_{ln} mode, and

$$P_{ln}=\frac{m^2c^4}{32e^2}\frac{ab}{\pi}\omega\left[k+\frac{k_{ln}^2}{k}\right]\delta a_{ln}^2 \tag{33}$$

for the TM_{ln} mode. The initial state of the electron beam is chosen to model the injection of a continuous, axisymmetric electron beam with a uniform cross section; hence, we choose $\sigma_{\|}=1$ for $-\pi\le\psi_0\le\pi$ and $\sigma_{\perp}=1$ for $r_0\le R_b$.

The particular example we analyze is that of a 35-GHz amplifier employing an electron beam with an energy of 3.5 MeV, a current of 800 A, and an initial radius of 1.0 cm which propagates through a waveguide characterized by $a=9.8$ cm and $b=2.9$ cm. In order to obtain peak growth rates in the vicinity of 35 GHz we choose a wiggler field with an amplitude of 3.72 kG and a period of 9.8 cm, with an entry taper of $N_w=5$. For purposes of illustration, the first case we consider is that of a beam with zero momentum spread ($\Delta\gamma_z=0$). For all cases discussed in this work with $\Delta\gamma_z=0$ the choice of a tenth-order Gaussian algorithm in each of the coordinates (ψ_0, r_0, θ_0) was found to provide an accuracy of the order of 0.1%. The initial electron distributions in the axial phase space and beam cross section are shown in Fig. 1. Each dot in the illustration of the axial phase space describes a *phase sheet* composed of 100 electrons distributed throughout the cross section of the electron beam. Each *phase sheet*, therefore, represents a cross-sectional slice of the electron beam, which is chosen initially as shown in Fig. 1(b). Although each phase sheet is initially chosen to be identical, the subsequent evolution of the electron trajectories in the presence of the radiation field is followed self-consistently. It should also be remarked that the distribution shown represents a uniform electron beam. The nonuniformity in the positions of the electrons chosen by means of the Gaussian algorithm is compensated for by a nonuniformity in the weighting of the electrons.

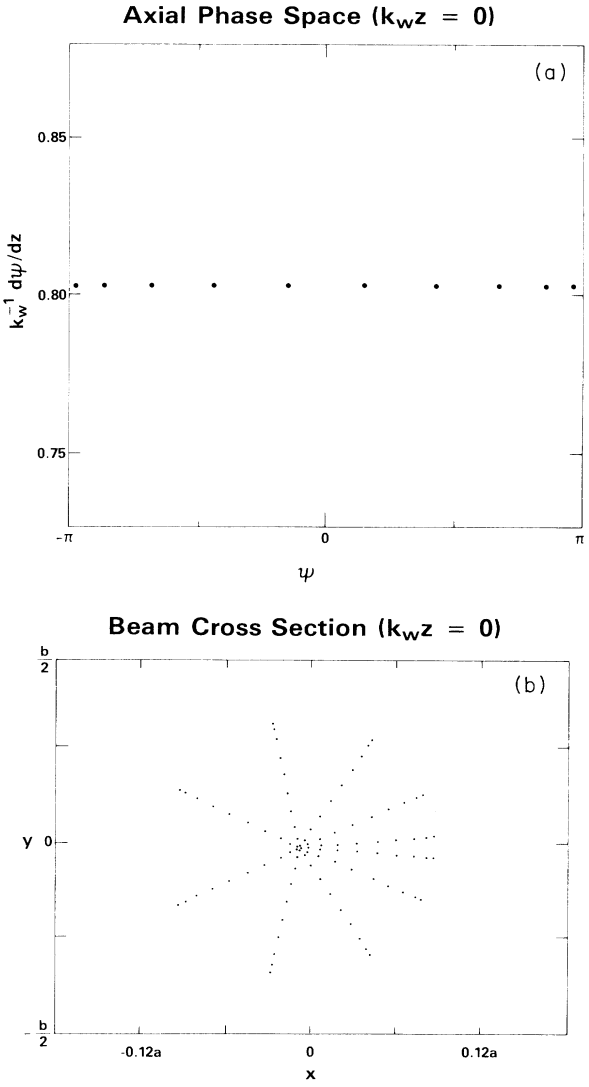

FIG. 1. Initialization of (a) the axial phase space, and (b) the beam cross section. Each point in the axial phase space represents the superposition of 100 particles distributed throughout the cross section of the beam.

There are three modes which are resonant in the vicinity of 35 GHz; specifically, the TE_{01}, TE_{21}, and TM_{21} modes. The analysis presented in this work deals with wave-particle interactions with single modes, and we shall deal with each of these modes individually. The first mode we treat is the TE_{01} mode which is the lowest-order resonant mode at the frequency of interest. The detailed evolution of the wave power as a function of axial position is shown in Fig. 2 for the injection of a 50-kW signal at a frequency of $\omega/ck_w=11.3$ (34.6 GHz). As shown in the figure, saturation occurs at $k_w z\simeq 115$ (1.79 m) at a power level of approximately 214 MW which corresponds to an efficiency of $\eta\simeq 7.75\%$. Wave amplification occurs principally within the uniform

wiggler region ($z > N_w \lambda_w$) which is 1.30 m for this case and yields an average gain of about 28 dB/m. Although this value for the average gain is lower than that observed in some other experiments (a gain of approximately 120 dB/m has been observed by Gold and coworkers[8]), the average normalized growth rate $\Gamma_{01}/k_w \simeq 0.05$ is quite high and is attributable to the relatively high wiggler amplitude and long wiggler period.

One feature of interest shown in Fig. 2 which merits some discussion is the oscillation in the instantaneous power which occurs with a period of $\lambda_w/2$. This is not found for the case of helical wiggler configurations for which the bulk transverse wiggler motion describes a helix with a transverse velocity of relatively constant magnitude. In contrast, a linearly polarized wiggler will induce a bulk wiggler motion in the plane normal to that of the wiggler field characterized by an oscillatory velocity. In order to illustrate this qualitatively, we observe that for the present configuration the bulk transverse wiggler motion is aligned along the x axis and varies approximately as

$$\mathbf{v}_w \sim \frac{\Omega_w}{\gamma_0 k_w} \sin(k_w z)\hat{\mathbf{e}}_x \ . \tag{34}$$

The source terms contained in the dynamical equations (16)–(19) are derived essentially from a calculation of $\langle \mathbf{J}\cdot\delta\mathbf{E} \rangle$; hence, the principal wave-particle coupling is with the x component of the radiation field. If we assume that $\delta E_x \sim \delta\hat{E}_x \sin(kz-\omega t)$, then it is evident that

$$\langle \mathbf{J}\cdot\delta\mathbf{E} \rangle \sim -\frac{\Omega_w}{2\gamma_0 k_w}\delta\hat{E}_x \langle \cos\psi - \cos(2k_w z - \psi) \rangle \ . \tag{35}$$

The interaction occurs when the ponderomotive phase is a slowly varying function of axial position [i.e., $\omega \simeq (k + k_w)v_z$], and the upper beat wave which varies as $\cos\psi$ describes wave amplification. The lower beat wave describes the oscillation at half the wiggler period. Although the spatial average of the contribution of the lower beat wave vanishes and this term provides no contribution to the bulk growth of the wave, the instantaneous values of the power are affected. Indeed, the instantaneous variation of the relative phase also exhibits an oscillation at half the wiggler period.

A full spectrum of the TE_{01} mode is shown in Fig. 3 in which we plot the saturation efficiency and distance to saturation as a function of frequency within the unstable band. As shown in the figure, wave amplification is found for frequencies extending from $\omega/ck_w \simeq 10$ (30.6 GHz) through $\omega/ck_w \simeq 14.2$ (43.5 GHz) with a peak efficiency of the order of approximately 9.8%. The peak growth rate (as measured by the distance to saturation) occurs for $\omega/ck_w \simeq 12.3$ (37.7 GHz), which is somewhat higher than the targeted 35 GHz. However, the gain bandwidth is sufficiently broad that the growth rate has not decreased significantly from the peak value.

The variation of the relative phase versus axial position is illustrated in Fig. 4 for $\omega/ck_w = 10.4$, 10.7, 11.0, 11.3, and 11.9. As is evident from the figure, the oscillation at one half the wiggler period is also manifested in the relative phase. The bulk variation (i.e., averaged over a wiggler period) shows the same qualitative behavior as that found for a helical wiggler.[26] Specifically, for frequencies at the low end of the gain band the relative phase decreases up to a point just short of the position at which the power saturates (indicated in the figure by an arrow), after which the phase remains relatively constant. As the frequency increases, the variation in the relative phase decreases until a critical frequency is reached ($\omega/ck_w \simeq 11$ for the particular case under consideration) for which the phase is found to vary little over the course of the interaction. This critical frequency is typically found to be about

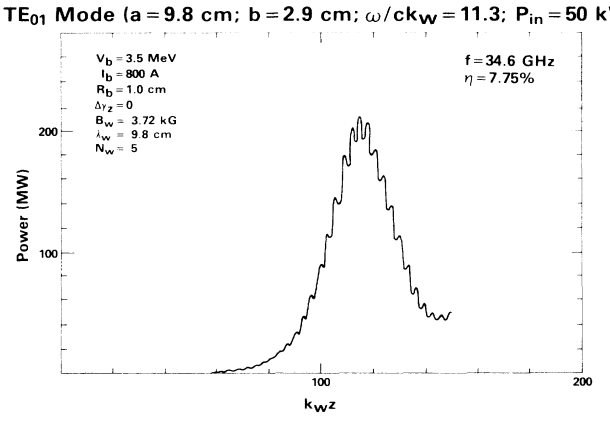

FIG. 2. Plot of the growth of the TE_{01} mode with axial position.

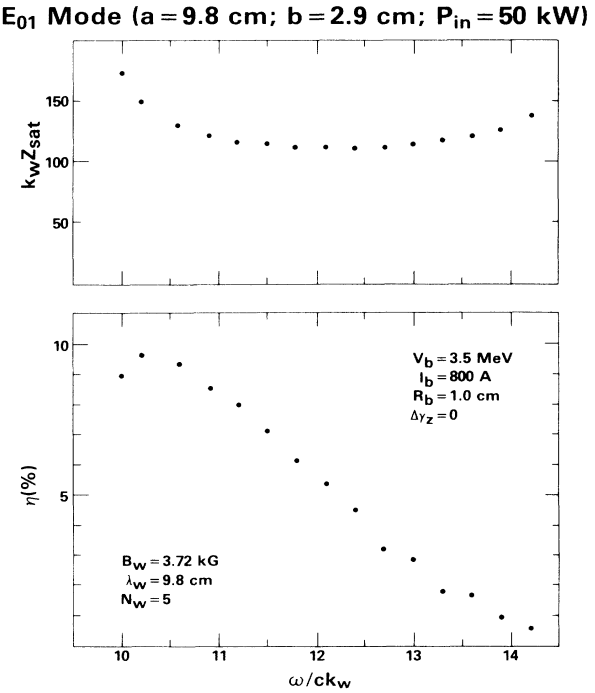

FIG. 3. Graph showing the distance to saturation and the efficiency of the TE_{01} mode as a function of frequency.

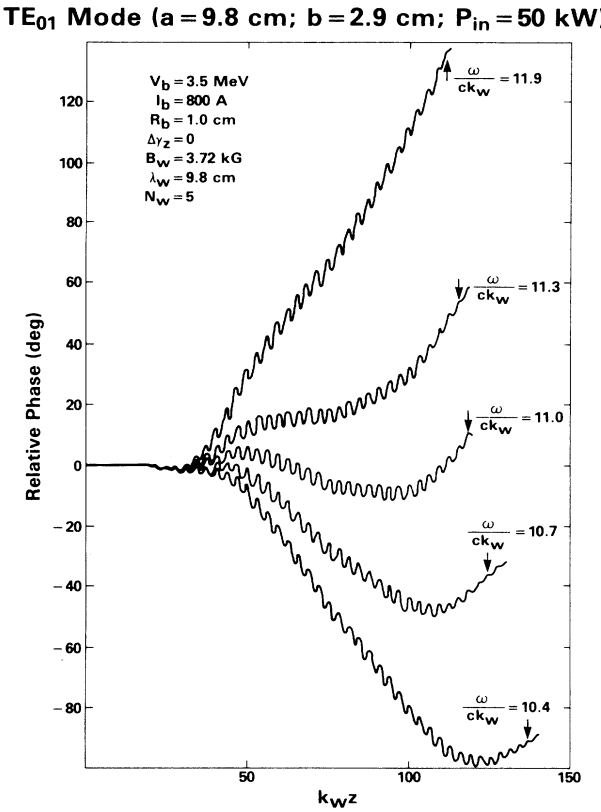

FIG. 4. Plot of the relative phase of the TE_{01} mode vs axial position for $\omega/ck_w = 10.4$, 10.7, 11.0, 11.3, and 11.9.

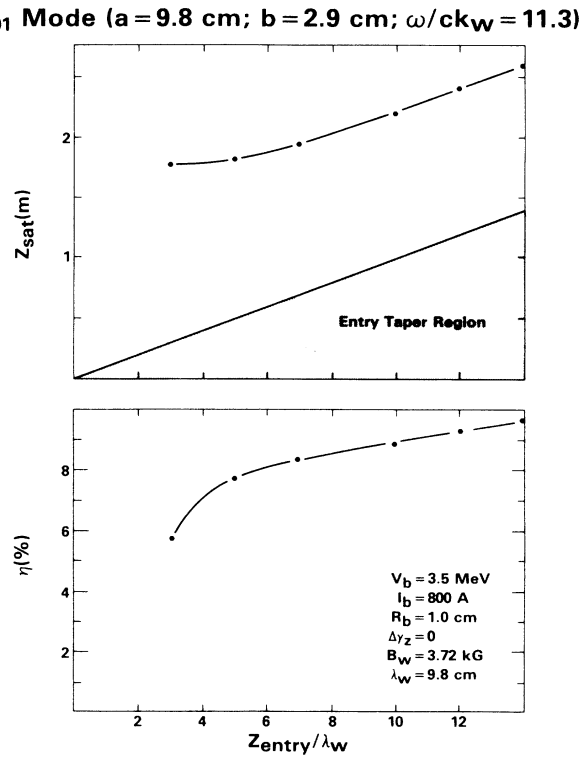

FIG. 5. Plot of the distance to saturation and the efficiency of the TE_{01} mode as a function of the length of the entry taper region for $\omega/ck_w = 11.3$.

10% below the frequency of peak growth. For frequencies above the critical frequency, the bulk phase increases monotonically. It should be remarked that the gain band under discussion corresponds to the upper frequency intersection between the beam resonance line $[\omega = (k + k_w)v_z]$ and the vacuum waveguide dispersion curve. There is also a gain band associated with the lower-frequency intersection which shows a similar variation in the relative phase, except, that there is an inversion in the frequency dependence.[26]

The question of the effect of the injection process of the electron beam can be addressed by varying the length of the entry taper region. The results of this analysis are shown in Fig. 5 in which we plot the saturation efficiency and the distance to saturation as functions of the length of the entry taper region for $N_w \geq 3$. We have arbitrarily chosen the minimum length of the entry taper region to be three wiggler periods since the fringing fields associated with the tapered wiggler field have been neglected, and we feel that below this value the fringing fields will be important. The results indicate that the saturation efficiency increases markedly as the length of the entry region increases from $3\lambda_w$ to approximately $6\lambda_w$, after which the increase in the efficiency becomes more gradual. We attribute this increase in the efficiency to a decrease in the effective momentum spread induced by the injection of the beam into the increasing wiggler field. It should also be noted that the increase in the distance to saturation is roughly linear for $N_w \geq 5$ and corresponds to the increase in the length of the entry region (i.e., the length of the uniform wiggler region remains relatively constant).

The particle dynamics during the course of the TE_{01} mode interaction are illustrated in Figs. 6 and 7. In the first place, we remark that saturation proceeds by means of the phase trapping of the beam in the ponderomotive potential. This is shown in Fig. 6 in which we plot the phase-space distribution of the beam at saturation. The dashed line in the figure represents an *approximate* separatrix calculated for particles at the beam center; hence, many of the electrons which appear outside of the separatrix may instead be on trapped particle orbits at the edge of the beam. The cross-sectional evolution of the beam is shown in Fig. 7. The cross-sectional projection of the beam at the start of the uniform wiggler region (i.e., $k_w z = 31$) is shown in Fig. 7(a). The bulk motion of the beam exhibits four essential features. The first is the primary wiggler-induced oscillatory notion which shifts the center of the beam off axis in the x direction, and this shift is clearly shown in Fig. 7(a). The second feature is that the transverse wiggler gradient introduces a betatron oscillation which causes a macroscopic scalloping of the beam envelope. In addition, on a microscopic level the

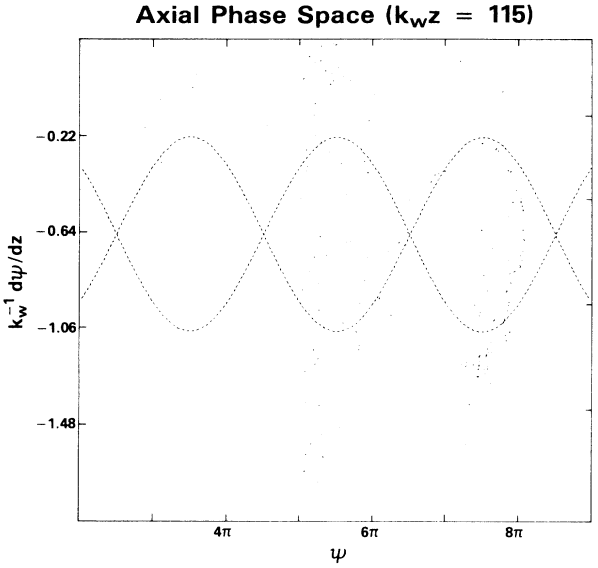

FIG. 6. Plot of the beam distribution in axial phase space at saturation.

individual electrons come into a focus and out again on the opposite side of the beam. This becomes evident in Fig. 7(a) by noticing that the two closely spaced "spokes" are oriented in the negative-x direction while in the initial state [Fig. (1b)] these same spokes were oriented in the positive-x direction. The third feature is that the transverse wiggler gradient also has a focusing effect on the beam which results in a reduction in the maximum beam radius relative to the initial state. The betatron oscillation occurs over a length of approximately $\Delta z_\beta \sim 3.08\lambda_w$ (i.e., $k_w \Delta z_\beta \simeq 19.3$), and the evolution of the beam cross section over this distance is shown in Fig. 7 (from $k_w z = 31-51$). Lastly, the geometry of the wiggler and the transverse gradients tends to distort the beam into an elliptical cross section. While this is evident in Fig. 7 at an early stage of the wiggler, it is shown even more dramatically in Fig. 7(f) which shows the cross section at saturation ($k_w z = 115$).

We now consider the TE_{21} mode, and plot the evolution of the wave power versus axial position in Fig. 8 for a 50-kW input signal at $\omega/ck_w = 11.3$ and an electron beam with a zero initial momentum spread. As is evident from the figure, the power saturates at $k_w z \simeq 104$ at about 194 MW for an efficiency $\eta \simeq 6.85\%$. In comparison with the TE_{01} mode, therefore, we conclude that the average growth rate is somewhat higher and the efficiency lower for the TE_{21} mode at this frequency. A complete spectrum for the TE_{21} mode is shown in Fig. 9 in which we plot the distance to saturation and the efficiency versus frequency. As shown in the figure, gain is found for frequencies ranging from $\omega/ck_w \simeq 8.9$ through $\omega/ck_w \gtrsim 14$ with a peak efficiency of approximately 12%. As a result, both the bandwidth and peak efficiency are higher for the TE_{21} mode than for the TE_{01} mode. In addition, while this frequency falls slightly below the frequency of peak growth rate for the TE_{01} mode, it is close to the frequency of maximum growth rate for the TE_{21} mode.

The evolution of the wave power versus axial position is shown in Fig. 10 for a 50-kW input signal in the TM_{21} model at $\omega/ck_w = 11.3$ and an electron beam with zero initial momentum spread. As shown in the figure, the power saturates at $k_w z \simeq 237$ with approximately 68.5 MW for an efficiency $\eta \simeq 2.45\%$. This is a much lower growth rate and efficiency than found for either the TE_{01} or TE_{21} modes, despite the fact that the cutoff frequency and dispersion curves are degenerate for the TM_{21} and TE_{21} modes. The difference between the two modes lies in the transverse mode structure. As mentioned previously, the principal component of the wiggler-induced motion is aligned with the x axis; hence, the wave-particle interaction is governed largely by the x component of the electric field. Comparison of the mode structures for the TE_{21} and TM_{21} modes given by Eqs. (4) and (5) shows that for a given mode amplitude (δA_{21}) the ratio of the x component of the electric field of the TM_{21} to that of the TE_{21} mode is approximately $2b/a \simeq 0.59$. As a result, the wave-particle coupling is weaker for the TM_{21} mode. Note that this conclusion would be reversed if the configuration were altered such that the principal component of the wiggler motion were aligned with the y axis. However, one effect arising from the degeneracy of the dispersion curves is that the frequency of interest ($\omega/ck_w = 11.3$) lies near to peak growth for both TE_{21} and TM_{21} modes. This is shown clearly in Fig. 11 in which we plot the distance to saturation and the saturation efficiency as a function of frequency for the TM_{21} mode. As might be expected, the reduced wave-particle coupling and growth rates for the TM_{21} mode result in a narrower bandwidth for instability, and we obtain wave growth for frequencies ranging from $\omega/ck_w \simeq 10.2-12$.

The question of the variation in the phase of FEL amplifiers has important implications for many of the potential applications of these devices. Since high powers and efficiencies have been demonstrated experimentally,[13] one such application may be as a high-power microwave source for the next generation of radio-frequency electron accelerators. However, one requirement for such an application is good phase stability of the output radiation against fluctuations in the electron-beam voltage. Examination of Fig. 4 shows that the relative phase at saturation varies rapidly with frequency. Since there is a correspondence between variations in the frequency at fixed voltage and variations in the voltage at fixed frequency, we might expect the phase at saturation to vary rapidly with beam voltage. This is indeed the case as shown in Fig. 12, in which we plot the relative phase at a fixed axial position (chosen to correspond to the saturation point for a beam voltage of 3.5 MeV) versus beam voltage for the TE_{01}, TE_{21}, and TM_{21} modes. The variation in the relative phase is approximately 51°/1% variation in the beam voltage for the TE_{01} mode, 43°/1% variation in the beam voltage for the TE_{21} mode, and 89°/1% variation in the beam voltage for the TM_{21} mode. Such rapid variations in the phase are consistent with results obtained previously for

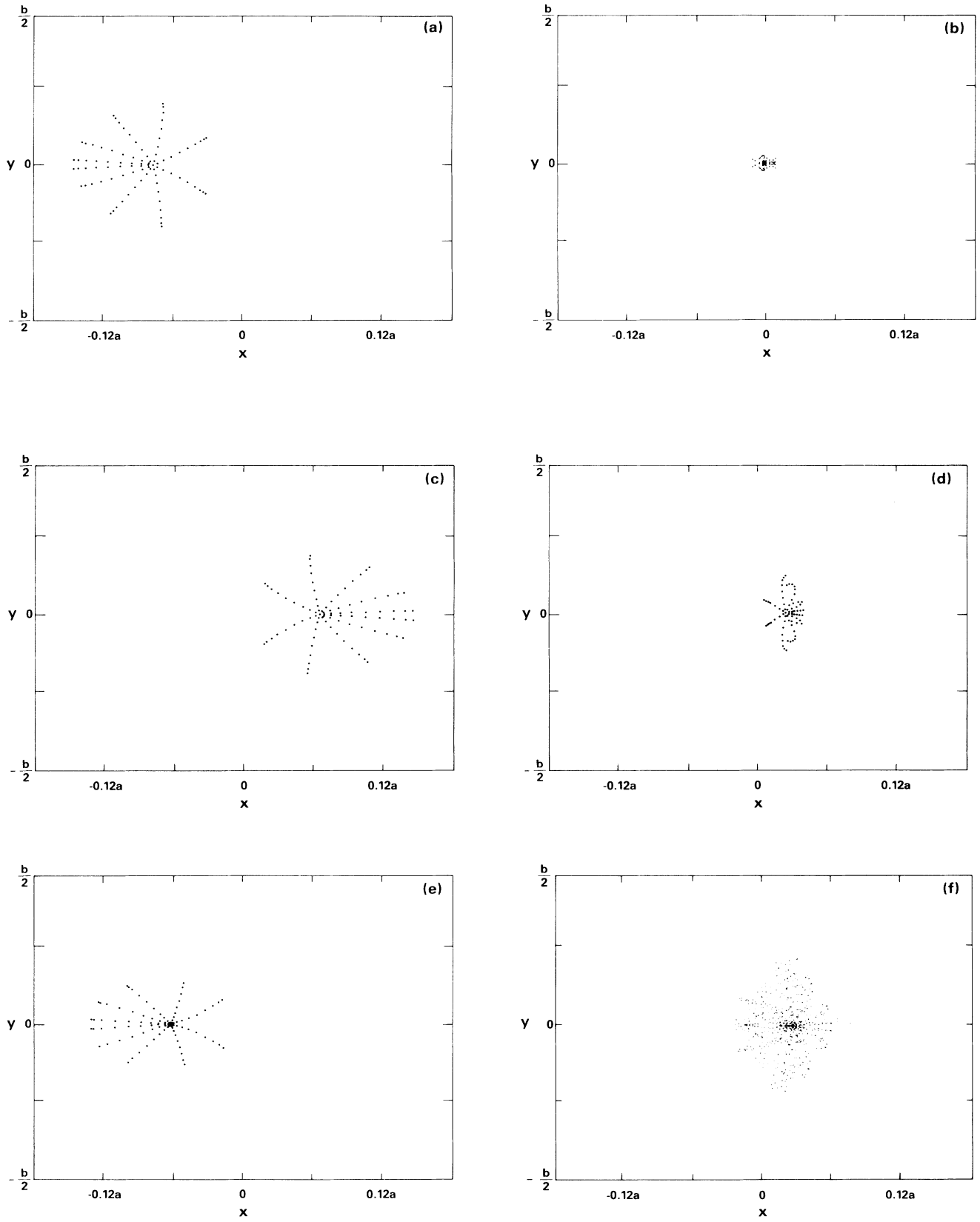

FIG. 7. Plot of the beam cross section at (a) the end of the entry taper region ($k_w z = 31$), (b) $k_w z = 36$, (c) $k_w z = 41$, (d) $k_w z = 46$, (e) $k_w z = 51$, and (f) $k_w z = 115$.

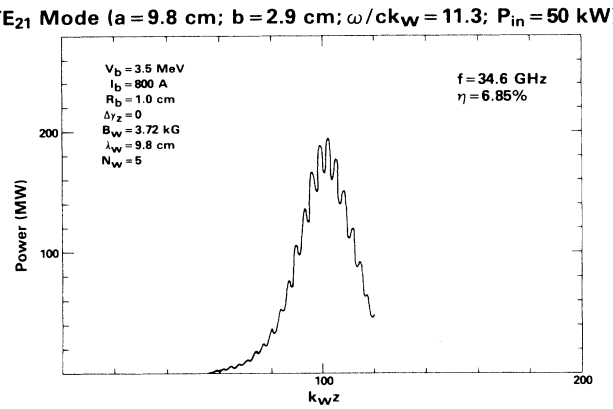

FIG. 8. Plot of the growth of the TE_{21} mode with axial position.

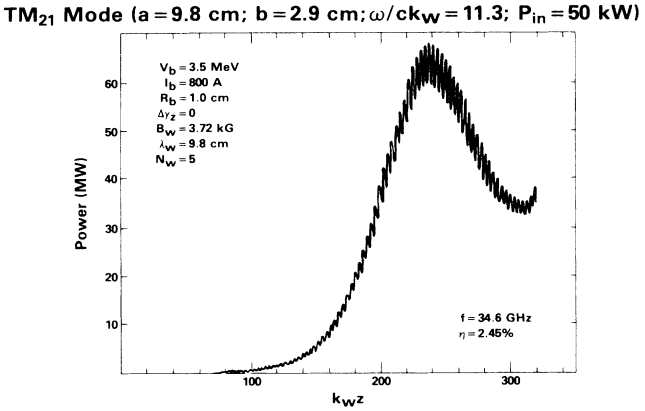

FIG. 10. Plot of the growth of the TM_{21} mode with axial position.

a helical wiggler, cylindrical waveguide configuration,[26] and contrasts with 8°/1% variation in beam voltage for a typical Stanford Linear Accelerator (SLAC) klystron.[30] We conclude, therefore, that applications which require an extremely phase-stable microwave source will also require an electron-beam source with a very low level of voltage fluctuations.

The effect of an initial momentum spread is shown in Fig. 13 in which we plot the efficiency versus $\Delta\gamma_z/\gamma_0$ for the TE_{01}, TE_{21}, and TM_{21} modes. From the beam-resonance condition, it is apparent that the transition to a thermally dominated regime occurs when $\Delta v_z / v_0 \sim \Gamma_{\ln} / (k + k_w)$. Making use of Eq. (22) we find that this transition occurs at about $\Delta\gamma_z/\gamma_0 \simeq 18\%$ for the TE_{01} and TE_{21} modes, and $\Delta\gamma_z/\gamma_0 \simeq 8\%$ for the TM_{21} mode. As a consequence, the cases shown in Fig. 19 are well short of the thermal-beam regime. The efficiency is found to decrease in an approximately linear fashion with increasing $\Delta\gamma_z$ for each of these modes, which corresponds with results ob-

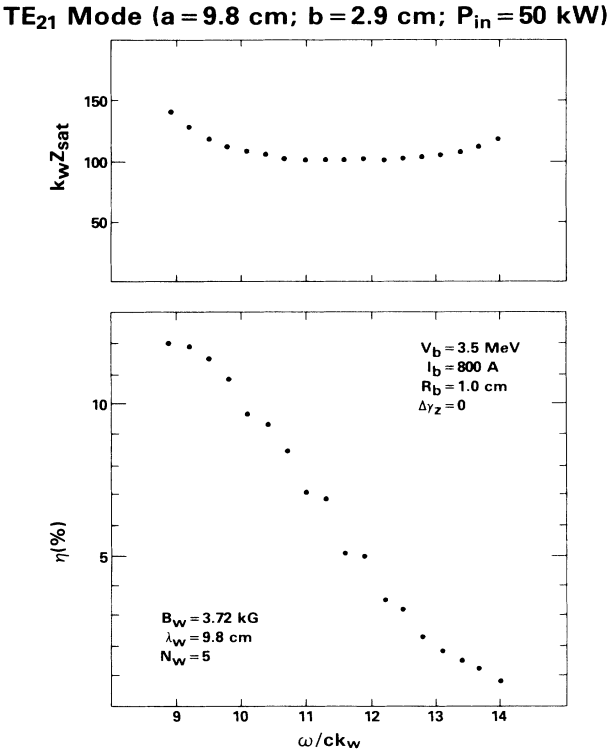

FIG. 9. Graph showing the distance to saturation and the efficiency of the TE_{21} mode as a function of frequency.

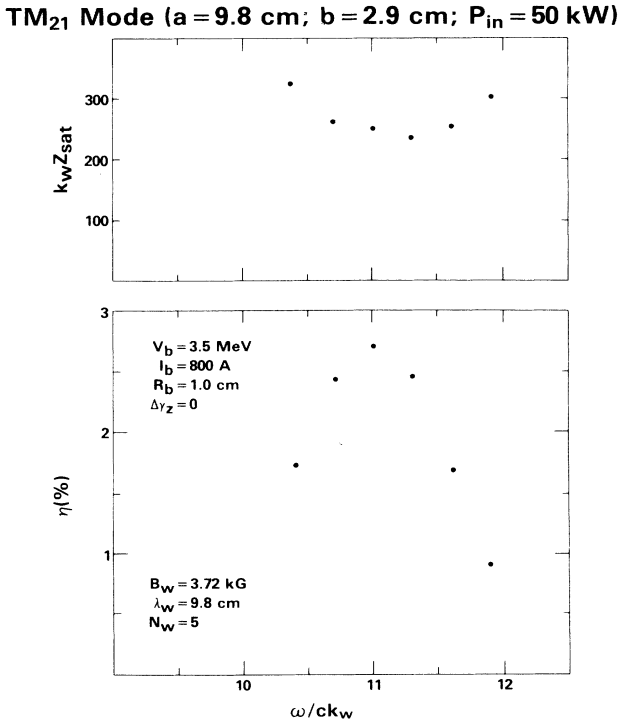

FIG. 11. Graph showing the distance to saturation and the efficiency of the TM_{21} mode as a function of frequency.

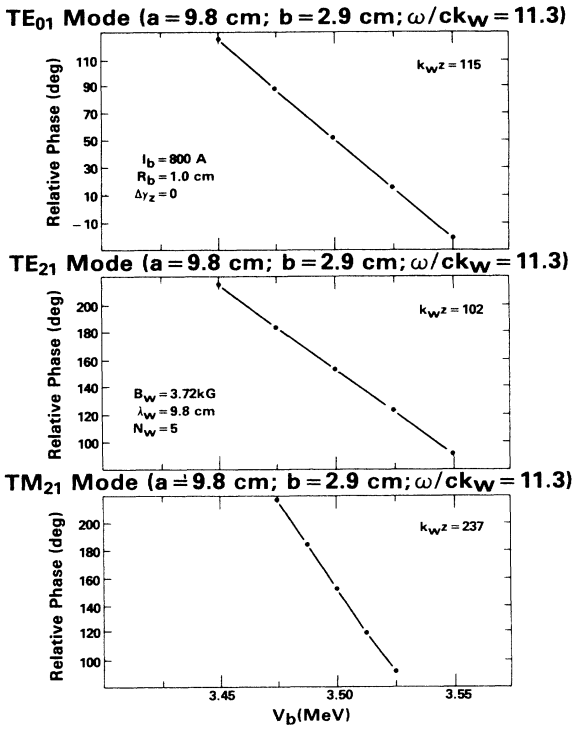

FIG. 12. Graph showing the variation in the relative phase at saturation (for $V_b = 3.5$ MeV) vs beam voltage.

tained for a helical wiggler configuration.[25] Note, however that the present results were obtained with the same model distribution (20) as for the helical wiggler, and the detailed variation in the efficiency with momentum spread can be expected to vary with the choice of distribution. Be that as it may, we find that the efficiency drops from $\eta \simeq 7.75\%$ to $\eta \simeq 4.98\%$ for the TE_{01} mode as $\Delta\gamma_z/\gamma_0$ increases to about 2.3%. For the TE_{21} mode, the efficiency drops from $\eta \simeq 6.85\%$ to $\eta \simeq 3.76\%$ as $\Delta\gamma_z/\gamma_0$ increases to 2.3%. The efficiency of the TM_{21} mode decreases from $\eta \simeq 2.45\%$ to $\eta \simeq 1.27\%$ as $\Delta\gamma_z/\gamma_0$ increases to 1%. This is more rapid than for the TE_{01} and TE_{21} modes, and occurs because the transition to the thermal-beam regime is found for a lower value of the momentum spread for the TM_{21} mode.

The scaling of the saturation efficiency with beam current for the TE_{01}, TE_{21}, and TM_{21} modes is shown in Figs. 14–16, respectively, for $\Delta\gamma_z = 0$ and $\Delta\gamma_z/\gamma_0 = 1\%$. On the basis of an idealized one-dimensional model,[29] it has been shown that the saturation efficiency should scale as $\eta \sim I_b^{1/3}$ for frequencies corresponding to peak growth rates. As shown in Fig. 14, this type of scaling law is obtained for the TE_{01} mode over a range of currents extending from approximately 300–1000 A. Observe that the dielectric effect of the electron beam on the waveguide mode is included in the formulation, and the bandwidth of the interaction shifts with the beam current. As a consequence, the increasing divergence between the simulation results and the scaling law for currents below 300 A is attributed to a shift in the frequency of peak growth away from $\omega/ck_w \simeq 11.3$. It should also be noted that the curve for $\Delta\gamma_z/\gamma_0 = 1\%$ increases with current only *slightly* faster than that obtained for $\Delta\gamma_z = 0$ and, other parameters being equal, the $I_b^{1/3}$ scaling law seems to be relatively in-

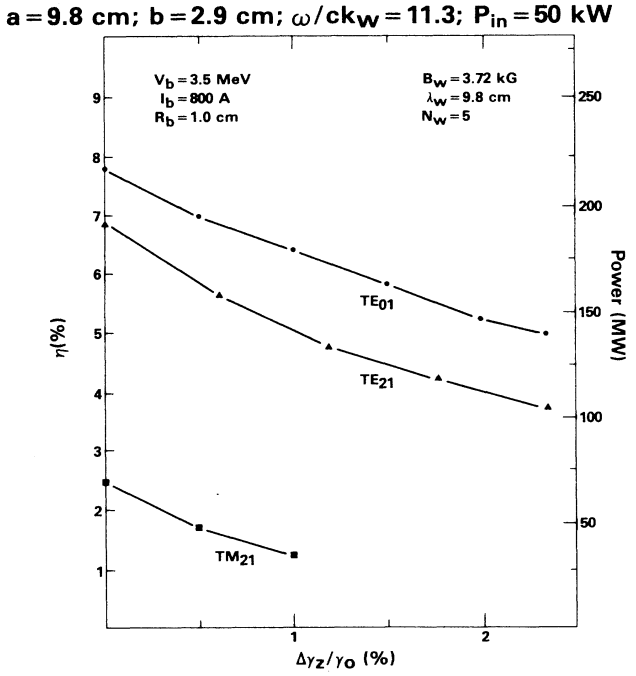

FIG. 13. Plot of the saturation efficiencies of the TE_{01}, TE_{21}, and TM_{21} modes vs axial energy spread for $\omega/ck_w = 11.3$.

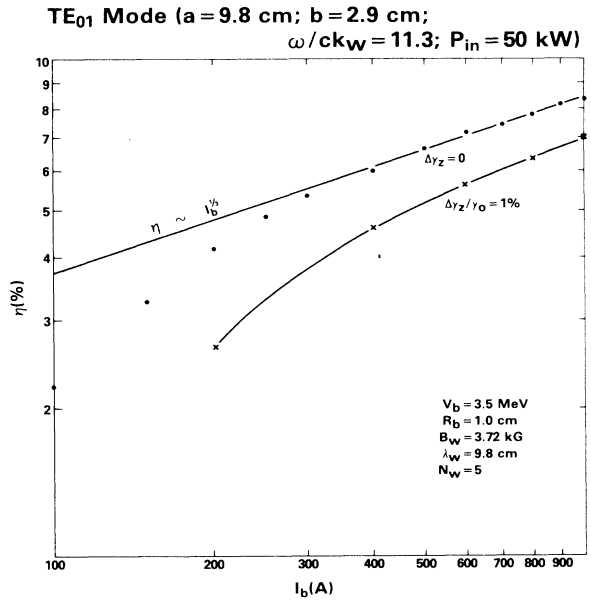

FIG. 14. Graph of the saturation efficiency of the TE_{01} mode vs beam current for $\omega/ck_w = 11.3$.

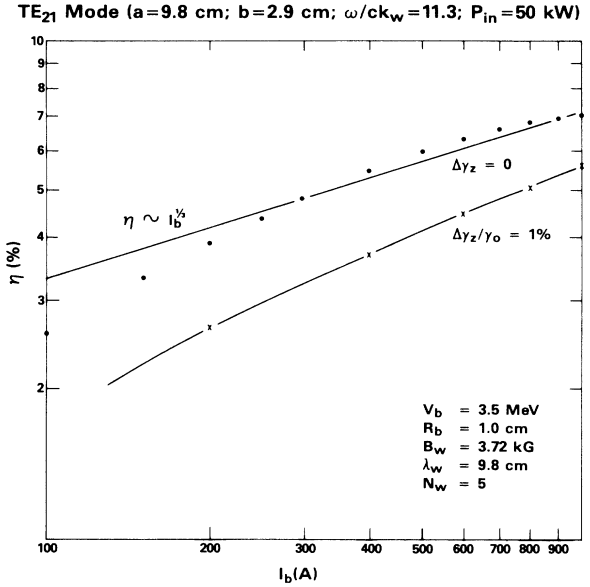

FIG. 15. Graph of the saturation efficiency of the TE_{21} mode vs beam current for $\omega/ck_w = 11.3$.

dependent of the momentum spread. However, one point of caution is worth noting in regard to these conclusions. Specifically, if the variation in current were accompanied by variations in the momentum spread and/or beam radius (as might be expected if the beam were held at constant brightness), then the scaling law might differ. The $I_b^{1/3}$ scaling law is also approximately found for the TE_{21} mode for currents ranging from about 200–1000 A. The slightly larger range of currents over which the scaling law seems to hold for the TE_{21} mode is attributed to the previously mentioned result that $\omega/ck_w = 11.3$ is closer to the frequency of peak growth rate for this mode than for the TE_{01} mode. As a consequence, this frequency remains in the vicinity of the maximum growth rate over a broader range of currents for the TE_{21} mode. Although the expected scaling law is approximately obtained for the TE_{01} and TE_{21} modes, three-dimensional effects involved in the beam propagation and the coupling between the beam and the transverse mode structure do modify the scaling. This is most evident for the TM_{21} mode shown in Fig. 16 for which we find the efficiency increasing somewhat faster than $I_b^{1/3}$.

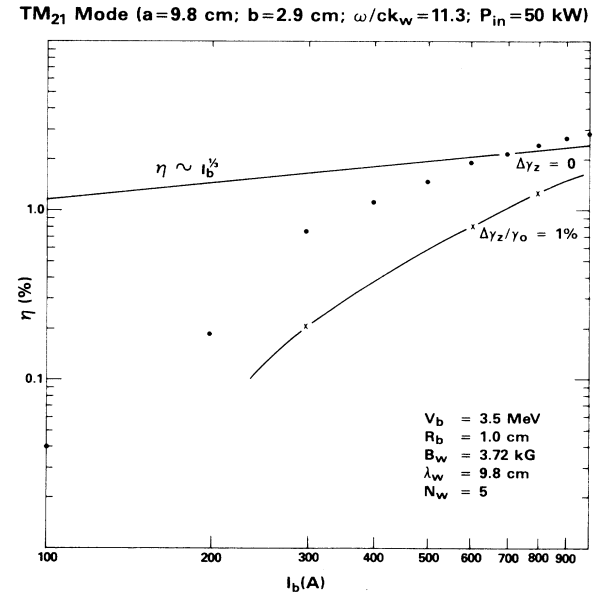

FIG. 16. Graph of the saturation efficiency of the TM_{21} mode vs beam current for $\omega/ck_w = 11.3$.

We now address the issue of efficiency enhancement by means of a tapered wiggler field, and concentrate on the TE_{01} mode. The fundamental theory of the efficiency enhancement mechanism has been amply discussed in the literature.[31–38] In order to understand the physical basis of the process, we observe that the wave-particle resonance condition which gives rise to amplification is extremely sensitive to the axial electron velocity. However, the axial velocity decreases as the wave is amplified until, ultimately, the resonance condition is broken and the amplification ceases. The purpose of the tapered wiggler field is to reduce the transverse velocity induced by the wiggler which, in turn, results in an axial acceleration that maintains the resonance condition. Thus, the tapered field is a means of "tapping" the transverse kinetic energy of the beam. This can be accomplished by a tapering of either the wiggler amplitude or period; however, in the present work we shall confine ourselves to a tapered amplitude configuration. The results of the simulation are in qualitative agreement with those obtained for a helical wiggler configuration,[24] and indicate that the efficiency enhancement is extremely sensitive both to the point at which the taper is begun and to the slope of the taper. The optimal position at which to begin the taper is, typically, at a point shortly prior to saturation (for the untapered system) which corresponds to the trapping of the bulk of the electron beam in the ponderomotive potential formed by the beating of the wiggler and radiation fields.

For the case corresponding to the TE_{01} mode shown in Fig. 2, the optimal point at which to begin the taper occurs for $k_w z_0 \simeq 110$. In order to accelerate the beam in the axial direction the wiggler field must be decreased, and the evolution of the wave power versus axial position is shown in Fig. 17 for a taper of $\epsilon_w = -0.007$. The efficiency enhancement (as measured by the growth in the wave power) continues for as long as the taper is maintained, and a maximum efficiency of $\eta_{\max} \simeq 34.0\%$ is obtained if the wiggler field is tapered to zero at $k_w z \simeq 253$ (i.e., 3.95 m). The effect of different choices for the wiggler taper is shown in Fig. 18, in which we plot the maximum efficiency found by tapering the wiggler field to zero versus ϵ_w. As shown in the figure, optimal results are found for $\epsilon_w \simeq -0.002$ at which point $\eta_{\max} \simeq 44\%$ and the interaction region extends to $k_w z \simeq 610$ (i.e., 9.5 m). The variation in the relative phase for a tapered wiggler interaction is shown in Fig. 19, in which we plot the rela-

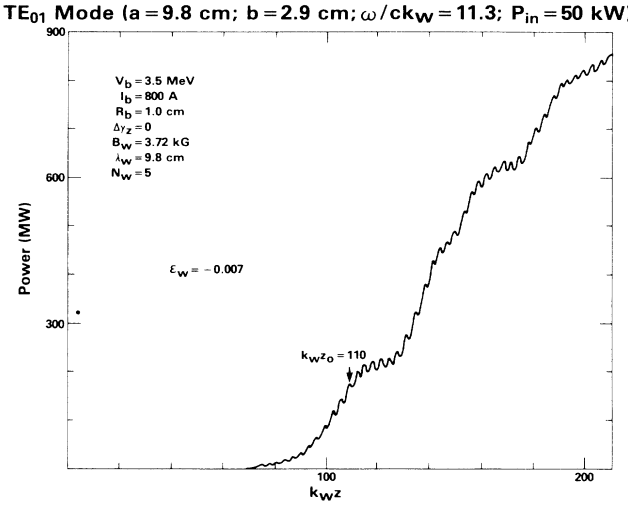

FIG. 17. Plot of the evolution of the TE_{01} mode for a tapered wiggler interaction with $\epsilon_w = -0.007$ and $k_w z_0 = 110$.

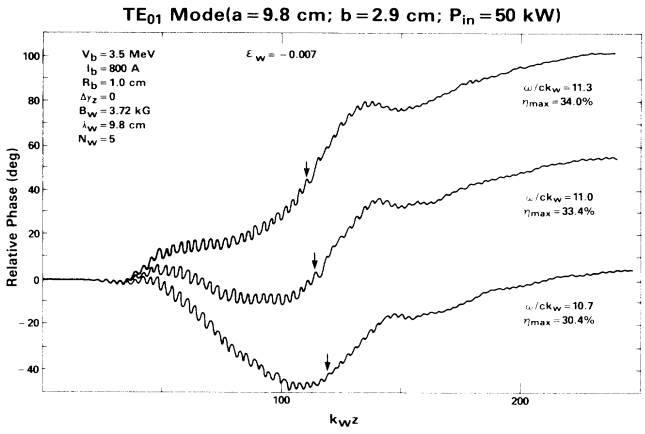

FIG. 19. Plot of the evolution of the relative phase during the course of the tapered wiggler interaction for $\omega/ck_w = 10.7$, 11.0, and 11.3.

tive phase versus axial position for $\epsilon_w = -0.007$, and $\omega/ck_w = 10.7$, 11.0, and 11.3. Note that the start taper point is chosen to be the optimum value for each frequency, and is indicated in the figure by the arrow. Three features are readily apparent from the figure. The first is that the variation in the relative phase subsequent to the start-taper point is approximately the same for each of the three frequencies shown, and the spacing between the curves remains approximately constant. Second, while the phase variation within the tapered wiggler region initially increases immediately after the start-taper position, the phase variation appears to saturate and remain relatively constant over an extended interaction length. Third, the oscillations at one-half the wiggler appear to decrease in amplitude over the course of the tapered wiggler region.

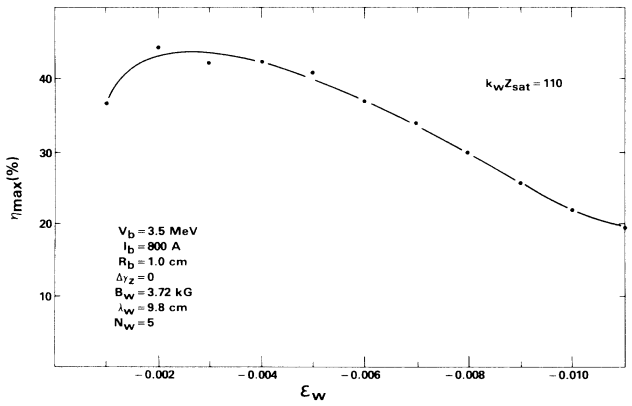

FIG. 18. Graph of the maximum efficiency of the TE_{01} mode vs wiggler taper (ϵ_w).

The effect of an initial beam momentum spread on the tapered wiggler-efficiency enhancement process has also been investigated, and the results are summarized in Fig. 20 in which we plot the maximum realizable efficiency (if the wiggler field is tapered to zero) versus $\Delta\gamma_z/\gamma_0$. The maximum efficiency at a fixed start-taper point ($k_w z_0 = 110$) chosen to correspond to the optimum position for $\Delta\gamma_z = 0$ is shown in Fig. 20(a) versus the axial

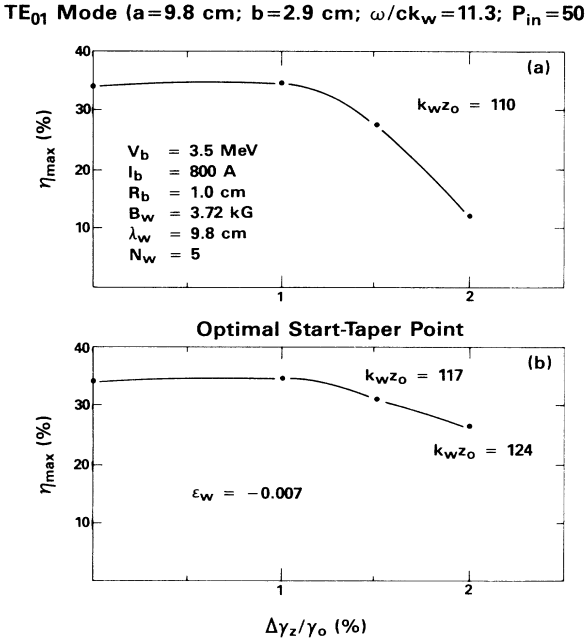

FIG. 20. Illustration of the effect of beam momentum spread on the tapered wiggler interaction at (a) fixed z_0, and (b) variable z_0. Observe that in (b) the optimal start-taper points correspond to $k_w z_0 = 110$ for $\Delta\gamma_z/\gamma_0 \leq 1\%$, $k_w z_0 = 117$ for $\Delta\gamma_z/\gamma_0 = 1.5\%$, and $k_w z_0 = 124$ for $\Delta\gamma_z/\gamma_0 = 2\%$.

momentum spread. As is evident from the figure, the efficiency-enhancement process is unaffected by the momentum spread for $\Delta\gamma_z/\gamma_0 \lesssim 1\%$, but decreases rapidly for axial energy spreads above this value. There are two principal reasons for this decrease in $\eta_{\max}$. The first is that the phase-trapping mechanism becomes less effective as the momentum spread increases because a proportionally greater fraction of the beam remains outside the trapped orbit region of the axial phase space. The second reason is that the increase in the momentum spread results in a decrease in the growth rate and a longer distance to saturation. Because of this, the optimum start-taper point is an increasing function of the momentum spread. Thus, if we determine the optimum start-taper point versus $\Delta\gamma_z$, then the maximum efficiency can be expected to decrease less rapidly with axial energy spread than is shown in Fig. 20(a). This is indeed the case, as shown in Fig. 20(b) in which we plot $\eta_{\max}$ versus $\Delta\gamma_z$ for the optimum start-taper points. Note that for $\Delta\gamma_z/\gamma_0 \lesssim 1\%$ this point coincides with that for $\Delta\gamma_z = 0$ (for the current choice of parameters). As seen in the figure, $\eta_{\max} \simeq 26.6\%$ for $\Delta\gamma_z/\gamma_0 = 2\%$ and a start-taper point of $k_w z_0 = 124$. This contrasts with an $\eta_{\max} \simeq 11.8\%$ (and $\Delta\gamma_z/\gamma_0 = 2\%$) when $k_w z_0 = 110$. As a consequence, we conclude that although the untapered efficiency decreases relatively quickly with increasing momentum spread, the tapered-wiggler interaction can accept a small level of momentum spread without suffering a significant degradation in the interaction efficiency. However, the upper limit on the allowable momentum spread must be determined by the particular choice of experimental parameters, and the value of $\Delta\gamma_z/\gamma_0 \lesssim 1\%$ should not be construed to be a general result.

IV. SUMMARY AND DISCUSSION

In this paper a fully self-consistent nonlinear theory and numerical simulation has been developed for the FEL amplifier in three dimensions. The particular configuration of interest consists of a cylindrically symmetric electron beam of arbitrary cross section (on entry at $z = 0$) injected into a loss-free rectangular waveguide in the presence of a linearly polarized wiggler magnetic field. The wiggler-field model is that generated by a magnet stack in which the individual magnets have parabolically tapered pole pieces in order to provide for electron focusing in the plane of the bulk wiggler-induced motion. In addition, the adiabatic injection of the electron beam is modeled by the inclusion of an initial taper of the wiggler amplitude. The system of equations derived is a generalization of a previously described analysis of a helical wiggler-cylindrical waveguide configuration[23–27] which treats the self-consistent evolution of the trajectories of an ensemble of electrons and the radiation fields. The analysis includes both the TE and TM modes, and includes the overlap of the transverse mode structure and the electron beam (i.e., the filling factor) in a self-consistent way. Space-charge fields have been neglected; hence, the analysis is restricted to the high-gain Compton (strong-pump) regime of operation. Since the problem of interest is the FEL amplifier, only single-frequency propagation is considered, which permits an average over a wave period to be performed that eliminates the fast-time-scale phenomena formulation. This results in a great increase in computational efficiency over a full-scale particle-in-all simulation code, and allows the application of the technique to short (i.e., optical) wavelengths given an appropriate mode structure.

The electron trajectories are integrated using the complete Lorentz-force equations, so we are able to study the detailed orbital dynamics in the combined wiggler-radiation field structure. The overall bulk motion of the electron beam exhibits a dominant oscillation at the wiggler period, as well as a slow-time-scale betatron oscillation due to the transverse inhomogeneity in the wiggler field. The dynamics of the adiabatic injection of the electron beam were studied by means of a comparison of the saturation efficiency with the length of the entry taper region. The results indicate that the saturation efficiency increases relatively quickly with the length of the entry taper region for $N_w \lesssim 6$, and more slowly thereafter. The reason for this is that the injection process itself in a realistic (i.e., three-dimensional) wiggler field introduces a effective momentum spread on the beam which decreases as the axial wiggler gradient becomes more gradual. For practical purposes $N_w \gtrsim 5$ appears to be an adequate compromise between the minimization of the overall wiggler length and the maximization of the interaction efficiency, and this is the regime in which many microwave FEL's have been operated.[4–8,10–12] In addition, the effect of a tapered wiggler amplitude on the enhancement of the interaction efficiency can be included in a straightforward manner.

The numerical analysis has been performed for the case of a 35-GHz FEL amplifier which employs a 3.5-MeV, 800-A electron beam with an initial radius of 1.0 cm. The beam propagates through a rectangular waveguide with dimensions $a = 9.8$ cm and $b = 2.9$ cm in the presence of a wiggler field with a 3.72-kG amplitude and 9.8-cm period. Three distinct waveguide modes are found to be amplified: the TE_{01}, TE_{21}, and TM_{21} modes. For this choice of frequency, the TE_{01} mode exhibits the highest (untapered) efficiency, while the TE_{21} mode has the highest growth rate. The wave-particle coupling for the TM_{21} mode is the weakest of the three modes and has the lowest growth rate and efficiency as well as the narrowest bandwidth. The effect of an initial momentum spread is investigated for axial energy spreads $\Delta\gamma_z/\gamma_0 \lesssim 2\%$ which, for this choice of parameters, is well within the cold-beam regime. Results indicate that over this range of $\Delta\gamma_z$ the efficiency decreases in an approximately linear fashion with increasing axial energy spread. This is in substantial agreement with the results obtained for a helical wiggler configuration;[25] however, it should be remarked that the same distribution has been used for both the planar and helical wiggler configurations. Thus, while the planar and helical wigglers behave in substantially the same manner, the detailed scaling of the efficiency with the momentum spread can be expected to vary with the detailed choice of distribution.

The phase variation of the planar wiggler configuration discussed herein is also in qualitative agreement with that

found for helical wiggler configurations.[26] The principal difference is that an oscillation at one-half the wiggler period is superimposed on the bulk variation in the phase due to details of the wave-particle coupling with a planar wiggler. Specifically, for the gain band associated with the upper (high-frequency) intersection between the beam-resonance line and the waveguide-dispersion curve, we observe that the bulk variation of the relative phase decreases with axial position up to a point short of that at which the power saturates for frequencies at the low end of the band. As the frequency increases, the phase variation decreases until a critical frequency is reached for which the phase remains relatively constant over the course of the interaction. This critical frequency has been found to occur at approximately 10% below the frequency of peak growth rate for all parametric cases studied for both the helical and planar wigglers. Above this critical frequency the average relative phase tends to increase with axial position. In view of the high power potential of the FEL amplifier, applications such as microwave sources for the next generation of radio-frequency electron accelerators are natural considerations and the question of the phase stability of these devices against fluctuations in the electron-beam voltage is of importance. Again, we find qualitative agreement on this issue between simulations of helical and planar wiggler configurations. The results indicate a much poorer phase stability than the current generation of SLAC klystrons, and we conclude that applications of FEL amplifiers which require an extremely phase-stable microwave source will also require an electron beam with a very low level of voltage fluctuations.

The enhancement of the interaction efficiency by means of a tapered wiggler amplitude shows maximum efficiencies of the order of 35–45 % are possible for this choice of parameters. This brings maximum power levels into the GW range. The simulation results also indicate that the tapered wiggler-efficiency-enhancement mechanism is relatively less sensitive to the effect of momentum spread than the uniform-wiggler case, and no degradation in the maximum efficiency is found for $\Delta\gamma_z/\gamma_0 \lesssim 1\%$ in the present case. Examination of the phase variation during the tapered wiggler interaction shows similar results over the entire gain band (Fig. 19), and there is no decrease in the phase separation for the various frequencies observed in the tapered wiggler region. Since variations in the frequency at fixed beam voltage are fundamentally equivalent to a variation in the voltage at fixed frequency (i.e., both processes *sweep* through the gain band), we find that our conclusion regarding the phase stability of FEL amplifiers is unaltered for the case of tapered wiggler interactions.

Indeed, the bulk features of the FEL interaction mechanism are found to be in substantial agreement for both helical and planar wiggler configurations. The most evident distinction is the rapid oscillation in both the power and relative phase which appears for planar wigglers at half the wiggler period. While the bulk wave amplification is unaffected by this oscillation, it may introduce an uncertainty in the measurement of the gain and/or power from planar wiggler configurations which is of the order of 10% (apart from systematic instrumental errors). In addition, the relative phase also exhibits this oscillation, which indicates a periodic modulation in wave refraction also occurs. It is, therefore, an open question whether this may affect the focusing (i.e., optical guiding) of the radiation, and this will be addressed in a future work by the inclusion of multiple modes in the formulation. However, this question may be moot for tapered wiggler configurations since the oscillation appears to be attenuated (Fig. 19).

Although the configuration described in this paper does not precisely coincide with the experiment conducted by Orzechowski and co-workers,[9,13] the parameters chosen for the numerical analysis coincide with those of the experiment and it is useful to compare the simulation with the experiment. The fundamental differences between the experimental configuration and the analytical model are that in the experiment (1) the beam was injected into the wiggler by means of an entry taper region one wiggler period in length, (2) a quadrupole field was used to provide electron focusing instead of parabolically shaped pole pieces, and (3) in the tapered wiggler experiment[13] the amplitude was tapered nonlinearly. A 50-kW 34.6-GHz (i.e., $\omega/ck_w = 11.3$) magnetron was used to drive the FEL amplifier, and the signal was injected in such a way as to couple primarily to the TE_{01} mode. As a result, the TE_{01} mode was the predominant component of the output signal; however, significant power levels were also detected in the TE_{21} and TM_{21} modes. The detailed experimental parameters we choose to compare with the experiment involve a 3.5-MeV, 850-A electron beam used in the tapered wiggler experiment. Although the beam is thought to exhibit a slightly elliptical cross section, the average of the semimajor and semiminor radii is about 1.0 cm and we choose this value for the beam radius in the numerical simulation. The waveguide and wiggler parameters are those used previously in Sec. III, and we note that since the fringing fields are not included in our model of the entry taper region the choice of $N_w = 5$ is a compromise. The evolution of the wave power in the TE_{01} mode as a function of axial position for these parameters is shown in Fig. 21 for a uniform wiggler ($\epsilon_w = 0$), and for $\epsilon_w = -0.007$. The results are similar to those described in the preceding section for an 800-A beam, and the best fit with the experiment is found for an axial energy spread of $\Delta\gamma_z/\gamma_0 \simeq 1\%$. As shown in the figure, the untapered wiggler results give a saturated power of 194 MW over a uniform wiggler-interaction region (i.e., $Z_{\rm sat} - 5\lambda_w$) of 1.4 m in length. This compares well with the experimental measurement of 180 MW over an interaction length of 1.3 m, and the discrepancies are within the experimental uncertainty. We remark, however, that the simulation results may be affected by as much as 20% by the choice of the length of the entry taper region. It is more difficult to compare the simulation (with a linear wiggler taper) and the experiment (with a nonlinear taper) in such a detailed fashion. It is certainly reasonable to expect that a nonlinear taper might be more efficient than a linear one in the sense that the efficiency enhancement can be accomplished over a shorter interaction region. Thus, in the comparison of the tapered wiggler results we interpret the simulation as an indication of limits on the energy extrac-

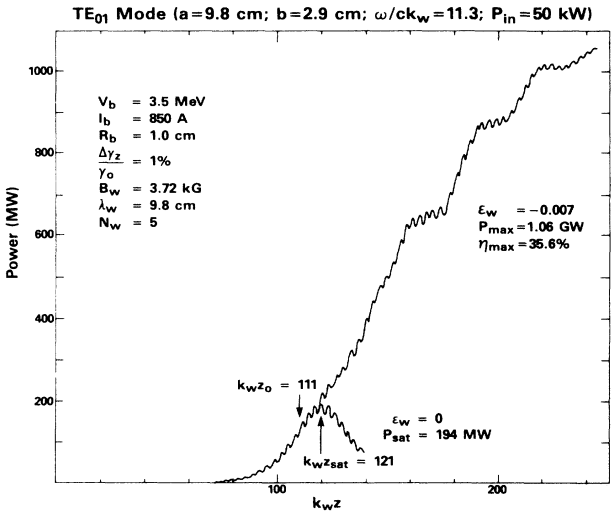

FIG. 21. Plot showing the evolution of the TE_{01} mode vs axial position for a uniform and tapered wiggler interaction.

tion. With this in mind we observe that the optimal start-taper point is at $k_w z_0 \simeq 111$ (slightly more than one wiggler period short of the saturation point for a uniform wiggler). We choose the slope of the taper to correspond roughly with the *average* taper in the experiment, and find a maximum efficiency of about $\eta_{\max} \simeq 35.6\%$ at a power level of 1.06 GW. This differs by only about 8% from that found in the experiment, and we interpret this as good agreement within the uncertainty introduced by the differences in the slope of the taper. We conclude, therefore, that the simulation is consistent with the interpretation of a 1% axial beam energy spread, which is supported by an electron-spectrometer measurement indicating an upper limit on the energy spread of 2%.[39] Furthermore, in view of the relative insensitivity of the tapered wiggler interaction (see Fig. 20), we conclude that the performance of the tapered wiggler experiment would not be markedly improved by a further improvement in beam quality (i.e., a decrease in the momentum spread).

It is useful to compare the analysis and simulation described herein with other models in order to assess the relative merits of the various formulations of the problem. To this end, we consider the simulation code FRED in use at the Lawrence Livermore National Laboratory[28,40] because this code has been used extensively to model and interpret the experiment. It is important to recognize that simulational models and computer codes undergo rapid development which renders an accurate description difficult; hence, I will confine my remarks to fundamental properties which include the particle dynamics and the treatment of the radiation field. The particle dynamics in FRED are treated in a reduced form by averaging the orbit equations over a wiggler period. The transverse motion is described in terms of the bulk wiggler and betatron oscillations by means of an analytical approximation, and the self-consistent effect of the radiation field on the transverse motion is not included. The dynamics in the axial direction are handled by integration of equations for the particle phase and energy. This is the most common approach used in the simulation of free-electron lasers and, as shown by the comparison between FRED and the experimental results,[9,13] it works well. However, certain effects are excluded from this formulation. First, we observe that the rapid oscillation at the second wiggler harmonic is lost entirely due to the averaging of the orbit equations over a wiggler period. Second, the injection of the electron beam into the wiggler is excluded from the simulation, and must be described explicitly. Third, because the self-consistent effect of the radiation field on the transverse electron motion is not included, the initial transients associated with the injection of the radiation into the amplifier are not properly handled. As a result, launching losses cannot be described by FRED, and the wave power must be initialized at a lower value than that actually injected into the amplifier.[9] Thus, it is our opinion that the approach to the particle dynamics described in this paper is superior to that employed in FRED. The advantage of FRED over the single-mode analysis we have described is that the radiation field is treated by means of a field solver which implicitly handles multiple modes and, thus, describes the optical guiding (i.e., focusing) of the radiation due to the electron-beam interaction. However, optical guiding can be treated via a multimode formulation of the present analysis as well. Indeed, such an analysis is now under study, and the results will be presented in the forthcoming work.

ACKNOWLEDGMENTS

This research was supported by the Office of Naval Research and the Office of Naval Technology. The authors would like to thank Dr. A. K. Ganguly, Dr. R. K. Parker, Dr. R. Sprangle, and Dr. R. H. Jackson for helpful discussions.

[1]R. M. Phillips, IRE Trans. Electron Dev. **7**, 231 (1960).
[2]V. L. Granatstein, S. P. Schlesinger, M. Herndon, R. K. Parker, and J. A. Pasour, Appl. Phys. Lett. **30**, 384 (1977).
[3]D. B. McDermott, T. C. Marshall, S. P. Schlesinger, R. K. Parker, and V. L. Granatstein, Phys. Rev. Lett. **41**, 1368 (1978).
[4]R. K. Parker, R. H. Jackson, S. H. Gold, H. P. Freund, V. L. Granatstein, P. C. Efthimion, M. Herndon, and A. K. Kinkead, Phys. Rev. Lett. **48**, 238 (1982).
[5]J. Fajans, G. Bekefi, Y. Z. Yin, and B. Lax, Phys. Rev. Lett. **53**, 246 (1984).
[6]J. A. Pasour, R. F. Lucey, and C. W. Roberson, in Free-Electron Generators of Coherent Radiation, edited by C. A. Brau, S. F. Jacobs, and M. O. Scully [Proc. Soc. Photo. Opt.-Instrum. Eng. **453**, 328 (1984)].
[7]J. A. Pasour, R. F. Lucey, and C. A. Kapetanakos, Phys. Rev. Lett. **53**, 1728 (1984).
[8]S. H. Gold, D. L. Hardesty, A. K. Kinkead, L. R. Barnett, and

V. L. Granatstein, Phys. Rev. Lett. **52**, 1218 (1984).
[9]T. J. Orzechowski, B. Anderson, W. M. Fawley, D. Prosnitz, E. T. Scharlemann, S. Yarema, D. Hopkins, A. C. Paul, A. M. Sessler, and J. Wurtele, Phys. Rev. Lett. **54**, 889 (1985).
[10]J. Fajans, G. Bekefi, Y. Z. Yin, and B. Lax, Phys. Fluids **28**, 1995 (1985).
[11]J. Masud, T. C. Marshall, S. P. Schlesinger, and F. G. Yee, Phys. Rev. Lett. **56**, 1567 (1986).
[12]J. Fajans, J. Wurtele, G. Bekefi, D. S. Knowles, and K. Xu, Phys. Rev. Lett. **57**, 579 (1986).
[13]T. J. Orzechowski, B. Anderson, J. C. Clark, W. M. Fawley, A. C. Paul, D. Prosnitz, E. T. Scharlemann, S. Yarema, D. B. Hopkins, A. M. Sessler, and J. Wurtele, Phys. Rev. Lett. **57**, 2172 (1986).
[14]L. R. Elias, W. M. Fairbanks, J. M. J. Madey, H. A. Schwettman, and T. I. Smith, Phys. Rev. Lett. **36**, 717 (1976).
[15]D. A. G. Deacon, L. R. Elias, J. M. J. Madey, G. J. Ramian, H. A. Schwettman, and T. I. Smith, Phys. Rev. Lett. **38**, 892 (1977).
[16]R. W. Warren, B. E. Newnam, J. G. Winston, W. E. Stein, L. M. Young, and C. A. Brau, IEEE J. Quantum Electron. **QE-19**, 391 (1983).
[17]M. Billandon, P. Ellaume, J. M. Ortega, C. Bazin, M. Bergher, M. Velghe, Y. Petroff, D. A. G. Deacon, K. E. Robinson, and J. M. J. Madey, Phys. Rev. Lett. **51**, 1652 (1983).
[18]J. M. Slater, J. L. Adamski, D. C. Quimby, T. L. Churchill, L. Y. Nelson, and R. E. Center, IEEE J. Quantum Electron. **QE-19**, 374 (1983).
[19]J. A. Edighoffer, G. R. Neil, C. E. Hess, T. I. Smith, S. W. Fornaca, and H. A. Schwettman, Phys. Rev. Lett. **52**, 344 (1984).
[20]B. E. Newnam, R. W. Warren, R. L. Sheffield, W. E. Stein, M. T. Lynch, J. S. Fraser, J. C. Goldstein, J. E. Sollid, T. A. Swann, J. M. Watson, and C. A. Brau, IEEE J. Quantum Electron. **QE-21**, 867 (1985).
[21]C. R. Pidgeon, S. D. Smith, W. J. Firth, D. A. Jorosynski, D. M. Tratt, J. S. Mackay, M. F. Kimmitt, J. M. Reid, M. G. Kelliher, M. W. Poole, G. Saxon, R. P. Walker, W. A. Gillespie, and P. F. Martin, IEEE J. Quantum Electron. **QE-21**, 1083 (1985).
[22]B. Levush, W. M. Manheimer, T. Antonsen, and P. Sprangle, Phys. Fluids **28**, 2273 (1985).
[23]A. K. Ganguly, and H. P. Freund, Phys. Rev. A **32**, 2275 (1985).
[24]H. P. Freund and A. K. Ganguly, Phys. Rev. A **33**, 1060 (1986).
[25]H. P. Freund and A. K. Ganguly, Phys. Rev. A **34**, 1242 (1986).
[26]H. P. Freund and A. K. Ganguly, IEEE J. Quantum Electron. (to be published).
[27]A. K. Ganguly and H. P. Freund (unpublished).
[28]E. T. Scharlemann, J. Appl. Phys. **58**, 2154 (1985).
[29]P. Sprangle, C. M. Tang, and W. M. Manheimer, Phys. Rev. A **21**, 302 (1980).
[30]R. W. Pierce, J. Jasberg, and J. V. Lebaqz, in *The Stanford Two-Mile Accelerator,* edited by R. B. Neal (Benjamin, New York, 1968), Chap. 10, p. 307.
[31]P. Sprangle, C. M. Tang, and W. M. Manheimer, Phys. Rev. Lett. **43**, 1932 (1979).
[32]N. M. Kroll, P. L. Morton, and M. N. Rosenbluth, in *Physics of Quantum Electronics: Free-Electron Generators of Coherent Radiation,* edited by S. F. Jacobs, H. S. Pilloff, M. Sargent, M. O. Scully, and R. Spitzer (Addison-Wesley, Reading, MA, 1980), Vol. 7, Chaps. 4 and 5.
[33]A. Szoke, V. K. Neil, and D. Prosnitz, in Ref. 32, Chap. 7, p. 175.
[34]D. Prosnitz, A. Szoke, and V. K. Neil, in Ref. 32, Chap. 21, p. 575.
[35]S. A. Mani, in Ref. 32, Chap. 22, p. 589.
[36]C. A. Brau and R. K. Cooper, in Ref. 32, Chap. 24, p. 647.
[37]J. M. Slater, J. Adamski, D. C. Quimby, W. M. Grossman, T. L. Churchill, and R. E. Center, in *Proceedings of the International Conference on Lasers '82,* edited by R. C. Powell (STS Press, McLean, VA, 1982), p. 212.
[38]P. Sprangle and C. M. Tang, Appl. Phys. Lett. **39**, 677 (1981).
[39]T. J. Orzechowski (private communication).
[40]W. M. Fawley, D. Prosnitz, S. Doss, and R. Galinas, in Free-Electron Generators of Coherent Radiation, edited by C. A. Brau, S. F. Jacobs, and M. O. Scully [Proc. Soc. Photo. Opt.-Instrum. Eng. **453**, 212 (1984)].

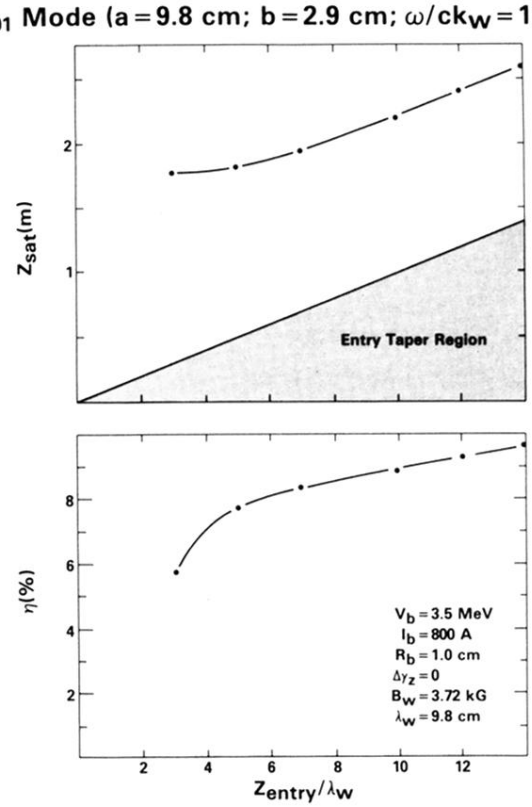

FIG. 5. Plot of the distance to saturation and the efficiency of the TE_{01} mode as a function of the length of the entry taper region for $\omega/ck_w = 11.3$.